

Comparison of models and lattice-gas simulations for Liesegang patterns

Lukas Jahnke and Jan W. Kantelhardt^a

Institute of Physics, Theory group, Martin-Luther-Universität Halle-Wittenberg, 06099 Halle, Germany

Abstract. For more than a century Liesegang patterns – self-organized, quasi-periodic structures occurring in diffusion-limited chemical reactions with two components – have been attracting scientists. The pattern formation can be described by four basic empirical laws. In addition to many experiments, several models have been devised to understand the formation of the bands and rings. Here we review the most important models and complement them with detailed three-dimensional lattice-gas simulations. We show how the mean-field predictions can be reconciled with experimental data by a redefinition of the distances suggested by our lattice-gas simulations.

1 Introduction

In recent years the general interest in self-organized structures is growing, triggered by the idea of cheap and fast production of nano-scaled devices. One of the promising effects for obtaining such devices is Liesegang pattern formation, based on a reaction-diffusion process. Experimental evidences for Liesegang patterns in solid materials on the nano-scale have already been obtained, see, e. g., [1,2,3]. For example, periodic patterns of silver nano particles in glass were observed by electron microscopy [1]. If it became possible to control the growth of such patterns with experimentally tunable parameters, self-organized optical devices could be made. In addition, the Liesegang phenomenon is an interesting research topic on its own due to the simple patterns arising out of complicated reaction and diffusion processes.

Since the first description of Liesegang rings in gels by the German chemist Raphael Eduard Liesegang in 1896 [4], many experiments and several models have been devised to understand the formation of the bands and rings. Although the basic problems are solved and four universal empirical laws have been found common to all experimentally observed Liesegang phenomena, there are still open questions. In literature misunderstandings regarding the exact definition of the measured quantities cause some discrepancies between the experimental results and the predictions of theoretical (mean-field) models. In this paper, we review the most important models for Liesegang pattern formation and complement them with extensive lattice-gas simulations of the reaction-diffusion processes. Based on our three-dimensional (3d) simulation results, we find a way to reconcile most experimental observations with the results obtained in mean-field models. In addition, we obtain evidence that fluctuations in 3d reaction-diffusion processes may play an important role in Liesegang pattern formation on the nano-scale.

The paper is structured as follows. Section 2 describes the main experimental findings, which can be summed up in four empirical universal laws describing the Liesegang patterns. Section 3 reviews previous work on models reproducing these laws. After an overview including a discussion of recent trends, we focus first on reaction-diffusion models with thresholds, and describe afterwards the spinodal decomposition model and a kinetic Ising model. Section 4 is

^a e-mail: jan.kantelhardt@physik.uni-halle.de



Fig. 1. (colour online) Experimental examples of Liesegang patterns in test tubes. Agent A is injected from the open end (top) of the tube, which contains agent B dissolved in a gel, yielding a linear geometry (Figure by D. B. Siano, <http://commons.wikimedia.org/wiki/Image:Liesegangrings.jpg>).

devoted to our studies based on lattice-gas simulations, presenting both the numerical method, the main findings, and a suggestion for reconciling the mean-field predictions with both, the experimental data and our 3d simulation results by a redefinition of the distances. Section 5 summarizes our findings and gives an outlook on further work on Liesegang pattern formation.

2 Experimental findings and empirical universal laws

In his original experiment, Liesegang covered a glass plate with a layer of gelatin impregnated with potassium chromate [4]. Then he added a small drop of silver nitrate in the centre. As a result, silver chromate was precipitated in the form of a series of concentric rings with regularly varying spacings. These rings became famous as Liesegang rings or more generally Liesegang patterns. Shortly after the first experiments, Wilhelm Ostwald presented an explanation for the occurrence of the rings [5], which is still the basis for most of the models today. The next important experimental findings followed several years later. In 1903, Morse and Pierce [6] investigated the formation time of the bands, observing diffusional dynamics, i. e., the time law. Jablczynski [7] showed twenty years later that Liesegang patterns follow a geometric series, i. e., the spacing law. Based on this observation Matalon and Packter [8,9] investigated the functional dependence of the positions of the bands on the concentrations of the reacting agents in 1955.

The geometry of the pattern depends on the initial conditions for the reacting agents. Usually one agent (the inner electrolyte), represented by the B particles in the models, is initially homogeneously distributed in the sample or gel. The second agent (the outer electrolyte), represented by the A particles, is injected. If A is injected in the centre, precipitation rings are formed. If B is homogeneously distributed in a cylindrical tube and A is injected from one end of the tube, bands form perpendicular to the motion of the reaction front, see Fig. 1. The second experimental setup is more appropriate for a theoretical description because it is effectively one dimensional (1d) [10]. Most of the theoretical and experimental work was done using this linear configuration; here we also focus on the 'band' setup. Although Liesegang rings are basically a projection of the bands onto polar coordinates, spiral patterns have been observed in the ring configuration exclusively. They have no equivalent in the linear configuration.

To define the basic observables, we assume that the n th band forms at time t_n at distance x_n from the side where A is injected. The width of the n th band is denoted by w_n . Firstly, the

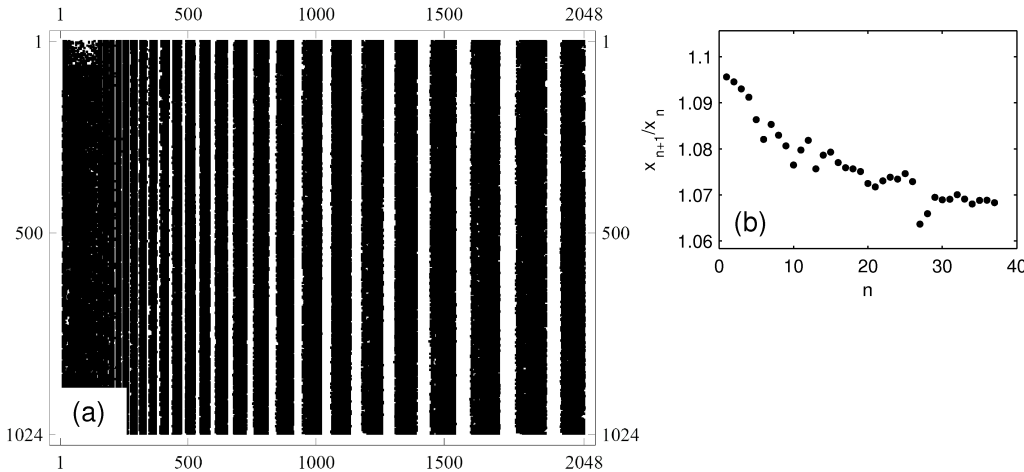


Fig. 2. Results of a 3d lattice-gas simulation of Liesegang band formation. (a) Injecting A from the left, Liesegang bands (black) with increasing distance form in the simulated lattice of $32 \times 32 \times 2048$ sites. To obtain the projection, all 32 two-dimensional slices were placed next to each other vertically. (b) The ratio x_{n+1}/x_n of the positions of the $(n+1)$ st and n th band is plotted versus n . See Fig. 6 in Sect. 4.3 for the parameters of the simulation.

position x_n is empirically found to be proportional to the square-root of the time t_n ,

$$x_n \propto \sqrt{t_n}. \quad (1)$$

This rule called *time law* in literature has been confirmed experimentally many times [6,11,12,13,14,15,16,17,18].

Figure 2 shows that the position x_n of the n th band follows approximately a geometric series converging to the *spacing law* [7]

$$x_n \propto (1+p)^n \Leftrightarrow x_{n+1}/x_n \rightarrow 1+p \quad \text{for large } n \quad (2)$$

with $p > 0$ the spacing factor. Typical empirical values for p reported in literature range from 0.05 to 0.4 [1,2,13,16,18,19].

A first systematic experimental analysis of the functional dependence of p on the concentrations of agents A and B was done by Matalon and Packter [8,9]. They gathered experimental results on p and found a functional dependence on the concentrations of both agents, a_0 and b_0 , respectively. This dependency is known as the *Matalon-Packter law* and takes the form

$$p = F(b_0) + G(b_0) \frac{b_0}{a_0}, \quad (3)$$

with F and G as dimensionless monotonously decreasing functions of b_0 [20]. F and G are not dependent on a_0 making p linearly dependent on $1/a_0$ for constant b_0 . This can serve as a test for the validity of the Matalon-Packter law. In Sect. 3.3.3 we will show that Eq. (3) is just an approximation of a more general law in the limit of reaction fronts much faster than the diffusion of the B particles. This limit holds for most of the experiments, because a_0 is usually much larger than b_0 while both electrolytes diffuse equally fast. An exception seems to be the experiment with nanoscale silver particles in glass [1] where the diffusion of silver ions, the inner electrolyte, might be one magnitude faster than the diffusion of the outer electrolyte, hydrogen. This leads to a slower motion of the reaction front compared to the diffusion of the silver ions.

As can be seen in Fig. 2(a) the Liesegang bands are getting broader for larger n . It is possible to set up an empirical law describing the width w_n of the n th band as function of the position x_n . Experimentalists use two competing versions of the *width law*,

$$w_n = \mu_1 x_n + \mu_2 \quad \text{and} \quad w_n \propto x_n^\alpha \quad (4)$$

see, e. g., [12,19,21] and [18,22,23,24], respectively. We are not aware of any papers comparing the two versions. In addition, different values of the exponent α in the second version have been published. The experiment with nanoscale silver particles in glass can be fitted by $\alpha \approx 0.7$ [1] (using the second version of Eq. (4)), but the results can be equally well fitted by the first version. Most other papers report larger values of α , e. g., $0.9 < \alpha < 1$ [24]. Publications of early reactive lattice-gas simulations, where the second version was first introduced, fit best with values of $\alpha \approx 0.5 - 0.6$ [22,25], but no comparison with the first version of Eq. (4) was done. It is difficult to distinguish between both versions of the width law because the number of bands is limited and the widths w_n of the bands are small compared to their positions x_n . Theoretical works prefer the second version with $\alpha = 1$ [18,23,24]. In Sect. 4.5 the different versions will be tested on our results of lattice-gas simulations. We will also propose an alternative, theoretically well grounded approach unifying both versions there.

The time law (1) is a simple consequence of a diffusion process. The position $x_f(t)$ of the reaction front between A and B moves proportional to \sqrt{t} with a prefactor that depends on a_0 and b_0 [26]. The other three laws cannot be explained so easily; one needs models describing nucleation and growth of the bands. These models can be categorized into two types. The first type is based on diffusion and reaction dynamics plus some thresholds which account for nucleation and growth. There exists a wide range of modifications. The second type of models uses well established phase separation techniques to explain the pattern formation based on spinodal decompositions [27] or a kinetic Ising model [28]. All of these models will be reviewed in the next section.

3 Models

3.1 Overview and recent trends

Reaction-diffusion models with thresholds are the oldest models describing Liesegang pattern formation. Only a few month after the first experiments by Liesegang, Ostwald gave a possible explanation of the pattern formation process on the basis of supersaturating liquids [5]. He suggested that the precipitation is not a result of a balanced reaction but must happen spontaneously when the concentration product K of the reactive partners reaches a critical concentration K_{sp} . The precipitation grows until K falls under a second concentration K_p . Both thresholds set the stage for several models differing in the detailed description of the reaction process. In principle they all follow a reaction scenario



and differ in the way the intermediate stage $\dots C \dots$ and the precipitation $\rightarrow D$ are described. For the concentrations of the different chemical agents A, B, \dots the symbols a, b, \dots will be used in the following.

The empirical laws described in the previous section became the basis for the theoretical work which started in the fifties. First analytical descriptions [29,30,31] showed that the patterns can be explained by diffusion and reaction processes with a moving reaction front. When numerical simulation became feasible about 90 years after the first experiments it was possible to reproduce patterns dynamically by studying the reaction-diffusion equations [14,21]. The fact that a novel approach was introduced in 1999 [23,27] shows that the Liesegang pattern phenomena are still an active research field in both, experiment and theory.

Apart from the novel simulation approach the trends in the literature follow two general lines. The first line works on an analytical description of the basic laws [24,32,33] or even looks for more general laws [34]. The second line varies the initial conditions and the geometrical configurations of the setup to understand the phenomena better and to find ways for applying the pattern formation in interesting engineering problems. Alternative geometries [35] and complex 3d boundary conditions [2,3,36] have been studied experimentally. Variation of the reaction terms [37], additional terms for a dissolution of the bands [15,38], as well as open systems [39] and, last but not least, systems with an additional electric field [15,40,41,42] have been studied

to vary the patterns. In very recent work the motion of the reaction front is even detached from the phase separation, which might be initiated, e. g., by a temperature gradient [43]. One hopes to understand and control the pattern formation process such that bands with constant distance can be generated, see [2,3] for experimental work in this direction.

Most of the theoretical work is based on an analytical study or numerical solution of differential equations. Since such equations are always based on the concentrations a, b, \dots of the reacting agents, they generally yield mean-field solutions. Although such mean-field solutions can reproduce the basic laws listed in the previous section they have two disadvantages. Firstly, they cannot account for the statistical character of the reactions. Hence, the influence of particle number fluctuations and thus the stability of the patterns cannot be investigated adequately. Although there are some ideas to include fluctuation by an additional noise term in mean-field models [2,40], we think that models with intrinsically statistical character are more adequate. This is particularly true for mesoscopic and nanoscopic systems, where fluctuations become more important. First experiments on microscopic scales indicate that fluctuations might play an important role [1,2,3]. Secondly, the differential equations may not describe the microscopical structure of the bands. Chopard *et al.* [22,25] proposed an alternative approach by taking the basic principles of the mean-field description and implementing them in a reactive lattice-gas simulation. Such simulations can be very helpful in reconciling mean-field predictions with experimental data, as we will see in Sect. 4. A similar approach seems also possible using Ising models [28].

In the following sections, the mentioned quantitative models and simulations will be reviewed, except for the lattice-gas simulations to be presented in Sect. 4.

3.2 Ion product saturation models

In the first and easiest quantitative models for Liesegang pattern formation, the ion product models, the precipitation takes place without an intermediate stage; i. e., there is no C stage in (5) [29,30,31]. Like in the Ostwald model, nucleation $A + B \rightarrow D$ occurs when the local product concentration $K = ab$ reaches the threshold K_{sp} . The precipitates of D will grow and deplete their surrounding of A and B . As the reaction front proceeds, the product concentration around the immobile precipitate decays until growth becomes impossible. Wagner [29], Prager [30] and Zeldovich *et al.* [31] could show that these ingredients yield patterns which obey the time law (1) and spacing law (2). The diffusion profiles of a and b are described by a system of coupled integro-differential equations with given boundary conditions. These equations can be rewritten in a more convenient way, if local coordinates are introduced in the form $\lambda_n = x_n/(2\sqrt{Dt_n})$ and $\gamma_n = x_n/x_{n-1}$. Taking $n \rightarrow \infty$ and $x_0 \rightarrow 0$ renders the equations mathematically solvable. The local coordinates $\lambda_n \rightarrow \lambda$ and $\gamma_n \rightarrow \gamma$ yield the time law and the spacing law, respectively. However, since these laws were the result of a continuous limit, the dynamics of the process was lost. Furthermore, the formation of the Liesegang bands was taken for granted and not proved by solving reaction-diffusion equations.

The first dynamical version of the ion product model proposed by Ross *et al.* [14] was deduced from the elementary chemical reaction $A + B \rightarrow D$ and solved numerically. Besides the typical diffusion terms for A and B ,

$$\partial_t a = D_A \partial_x^2 a - R \quad \text{and} \quad (6)$$

$$\partial_t b = D_B \partial_x^2 b - R \quad (7)$$

with diffusivities D_A and D_B , respectively, the equations include a reaction rate R constructed for a specific experimental configuration. In principle, R mimics an auto-catalytic growth process with a growth rate proportional to an increasing function of the supersaturation $S = (ab/K_{sp}) - 1$. The authors tested different power laws and exponential functions and observed pattern formation for a very quickly growing function $R(S)$ only. Beside the confirmation of the time law no quantitative observations of the other laws were reported.

Later Zrinyi *et al.* [44] pointed out that no detailed description of the agent transport is needed, since precipitation takes place on a faster time scale. It is thus possible to model the

growth process by a given critical threshold K_p . The corresponding source term for additional D can be written as a Heaviside step function, $c_1(a, b, d) \Theta(ab - K_p)$. The growth starts when the product concentration exceeds a second threshold $K_{sp} > K_p$, where the rate is independent of d . The partial differential equation for the precipitate concentration d can thus be written as [44,45]

$$R = \partial_t d = c_1(a, b, d) \Theta(ab - K_p) + c_2 \Theta(ab - K_{sp}), \quad (8)$$

where c_1 and c_2 are model-dependent functions of the parameters (initial concentrations and diffusion coefficients), and c_1 also depends on a , b and d . Liesegang patterns observed in a wide range of systems can be modelled this way. In particular, it was possible to show that the time law and the spacing law hold for a large set of parameters [44]. The Matalon-Packter law was confirmed only if the initial concentration of the outer electrolyte a_0 is sufficiently large. However, p was shown to stay a monotonously decreasing function of a_0 even if a_0 is small. Furthermore, p increases monotonously with K_{sp} in a non-linear way, and it is anti-proportional to the diffusivity D_A of the outer electrolyte. The results for a specific p do not depend on the individual parameters but on ratios of parameters with equal dimension – a simple consequence of the mean-field character of Eqs. (6) to (8). The findings are consistent with an experimental categorisation of the patterns by the product and the difference of the initial concentrations [13]. The width law, however, was not investigated.

In closely related approaches, growth was modelled proportional to the concentration of the precipitate, corresponding to $K_p = 0$ and $c_1 \propto d$ in Eq. (8) [32,33]. Focusing on the Matalon-Packter law (3), Antal *et al.* found that F is constant and $G \propto \sqrt{D_B/D_A} K_{sp}/b_0^2$ [32]. This result was achieved analytically based on the assumption $b_0 \ll a_0$; hence the failure of the Matalon-Packter law for low a_0 could not be observed. This result is inconsistent with $p \propto 1/D_A$ in [44], due to different assumptions for c_1 and c_2 . Lebedeva *et al.* searched for a criterion for the pattern formation [33], finding $\Phi = K_{sp} k_2 D_B / u^2(t) > 2 + \sqrt{5}$, with k_2 the growth rate and $u(t)$ the velocity of the front (decreasing with time). Patterns are thus formed when the nucleation threshold K_{sp} is high and the growth rate k_2 is large. The time dependence of $u(t)$ explains why patterns do not start at $x_0 = 0$ but an empty (“plug”) zone exists at the edge. The first two results match with those of Ross *et al.* [14] and Zrinyi *et al.* [44], who did not study the velocity of the reaction front.

3.3 Nucleation and growth models

The next models with slightly increased complexity separate the reaction-diffusion process $A + B \rightarrow C$ from the nucleation and growth process $C \rightarrow D$, introducing an intermediate state C , see Eq. (5). This, however, considerably simplifies the analysis. In the literature such models are often called nucleation and growth models because the formation of D depends on the nucleation and accumulation of C rather than on the product concentration of A and B .

This model was first introduced by Keller *et al.* [46] who analysed reaction-diffusion equations and confirmed the time law (1) and the spacing law (2). In contrast to Wagner and Prager [29,30] they could calculate the positions x_n of the bands without a priori assuming band formation and stopping of the band growth. The first numerical solutions for a nucleation and growth model were presented by Dee [21]. He used a similar technique as Ross *et al.* [14] (see previous section) and determined the nucleation and growth criterion by classical nucleation theory. A detailed work concerning the nucleation and growth of silver particles similar to Dee was presented recently [47]. Since the reaction-diffusion process can be separated from the precipitation process, we will discuss the two stages separately.

3.3.1 First process: reaction-diffusion $A + B \rightarrow C$

The simple reaction-diffusion process $A + B \rightarrow C$ is important independently of Liesegang patterns since it is a basic process in many chemical reactions. To apply the results to the Liesegang pattern phenomena we will focus on a quasi-1d geometry where the reacting particles

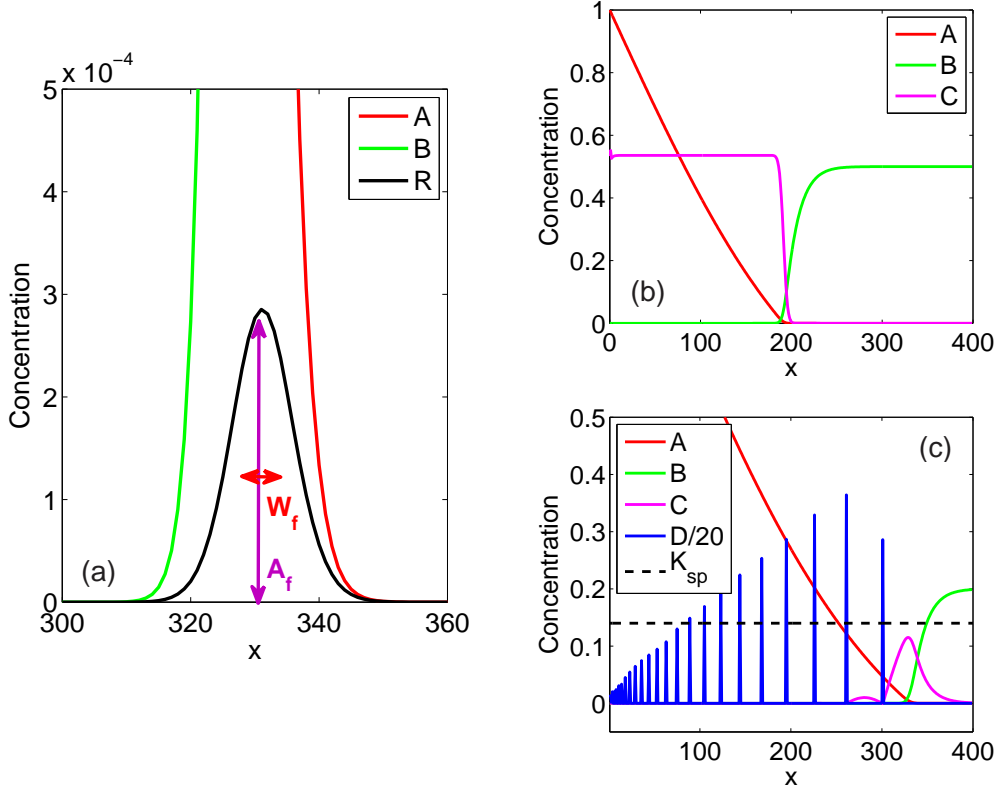


Fig. 3. (colour online) Illustration of the concentration profiles obtained in the reaction-diffusion process $A + B \rightarrow C$ without (a,b) and with (c) precipitation $C \rightarrow D$. The concentrations $a(x,t)$ (red) and $b(x,t)$ (green) are shown for fixed time t together with (a) the reaction rate $R(x,t) \propto ab$ (black) following Eq. (9), (b) the accumulated concentration $c(x,t)$ (magenta), and (c) the rescaled concentration of the precipitate D (blue). Note the constant value of $c(x,t) = c_0$ behind the reaction front in (b) according to Eq. (11). The dashed line in (c) indicates the threshold K_{sp} ; the next band is started when $c(x,t)$ reaches K_{sp} .

are separated at time $t_0 = 0$ with initial concentration a_0 and b_0 . The concentration profiles $a(x,t)$ and $b(x,t)$ for $x \geq 0$ and $t > 0$ are determined by the reaction-diffusion equations (6) and (7) with the initial conditions $a(x,0) = a_0\Theta(-x)$, $b(x,0) = b_0\Theta(x)$ [48]. The reaction term R is again assumed to be proportional to the concentration product $K = ab$. Under these assumptions it is possible to calculate $a(x,t)$ and $b(x,t)$ as well as the reaction rate $R(x,t) \propto ab$ asymptotically for large times t [49],

$$R(x,t) \sim A_f S_R \left[\frac{x - x_f(t)}{w_f(t)} \right], \quad (9)$$

where S_R is approximately a Gaussian [27,50]. The result is illustrated in Fig. 3(a). $R(x,t)$ describes the reaction front and reaches its maximum value at x_f which scales as $x_f(t) \sim \sqrt{t}$. The width of the front scales as $w_f(t) \sim t^\gamma$ with $\gamma = 1/6$. The production rate A_f of C at $x = x_f$ is proportional to $t^{-\zeta}$ with $\zeta = 2/3$. A scaling analysis regarding the impact of fluctuations [51] leads to the conclusion that the critical dimension, above which fluctuations become unimportant, is $d_c = 2$. In 2d logarithmic corrections apply and in 1d the whole dynamics change dramatically [51].

It is possible to approximate the effective diffusion coefficient D_f for the reaction front, i. e., the prefactor in $x_f = \sqrt{2D_f t}$ as well as the concentration c_0 of C behind the reaction front. This requires a few assumptions [52] which will be usually fulfilled in typical experimental setups.

The reaction front $R(x, t)$ has to be confined in a region (reaction zone) $x_f(t) - w_f(t)/2 < x < x_f(t) + w_f(t)/2$ for all times t , disregarding all reactions outside this region. Then the concentration profile of each agent can be written as a solution of a diffusion equation [26]. Furthermore, Eqs. (6) and (7) must be approximated by a quasi-stationary solution in the region $-(D_A t)^{1/2} \ll x \ll (D_B t)^{1/2}$. Under these conditions the effective diffusion coefficient D_f is given by an analytic implicit equation [52],

$$H\left(-\sqrt{\frac{D_f}{2D_A}}\right) = \frac{a_0\sqrt{D_A}}{b_0\sqrt{D_B}} H\left(\sqrt{\frac{D_f}{2D_B}}\right) \quad (10)$$

with $H(x) = [1 - \text{erf}(x)] \exp(x^2)$. Here, $\text{erf}(x)$ is the Gaussian error function defined as $\text{erf}(x) = \frac{2}{\sqrt{\pi}} \int_0^x \exp(-z^2) dz$. Evidently, the velocity of the reaction front does not depend on each of the initial concentrations, but on their ratio a_0/b_0 , and it scales in the same way as D_A and D_B , since no characteristic time and length scales exist. The same approximation also yields that the concentration of C behind the reaction front is constant (see Fig. 3(b)), given by [32]

$$c_0 = \frac{b_0}{\pi} \sqrt{\frac{2D_B}{D_f}} H^{-1}\left(\sqrt{\frac{D_f}{2D_B}}\right). \quad (11)$$

The interesting point of these results, for the Liesegang pattern phenomena, is that only c_0 and D_f are essential parameters. Since both depend only on the initial concentrations and the diffusion coefficients, the band formation is independent of the reaction rate which is hard to measure. This does not imply, however, that the width of the bands or the specific concentration profiles are independent of the reaction rate.

3.3.2 Second process: precipitation $C \rightarrow D$

Describing the $A + B \rightarrow C$ process exclusively by c_0 , D_f , and the Gaussian reaction front (9), we now focus on the precipitation step. Like Ross *et al.* [14] (see Sect. 3.2), Dee [21] modelled the precipitation process using the classical droplet theory. Droz *et al.* [24] showed that Dee's approach can be simplified into

$$\partial_t d(x, t) = c_1 N[c(x, t), d(x, t)] + c_2 \Theta[c(x, t) - K_{sp}] \quad \text{with} \quad N(c, d) \propto d(x, t), \quad (12)$$

corresponding to Eq. (8) with $K_p = 0$ and c_1 and c_2 constants or proportional to c . A typical result of such a simulation is shown in Fig. 3(c). Using this model, Dee confirmed the spacing law (2) and found the linear form of the width law (4). Due to limited computational resources he was restricted to one example with only six bands and obtained no information on the Matalon-Packter law (3).

In Eq. (12) the growth of the precipitates is restricted to the points of the nucleated particles, see also Fig. 3(c). To obtain bands with a macroscopic width w_n one would need nucleation at every point in w_n since no non-local term exist. Although no macroscopic width is reproduced in this model one sees that the height of the bands, which can be interpreted as their mass or integrated particle number, seems to grow linearly. This is in agreement with a theoretical prediction which will be introduced in Sect. 4.5.

Alternatively it would be possible to allow non-local growth such that C can become D in a broader surrounding of an initial nucleation centre. A popular version of the non-local term is [2,53]

$$N(c, d) = \Theta\left[\int_{x-dx}^{x+dx} d(x', t) dx'\right] \Theta[c(x, t) - K_p]. \quad (13)$$

In this case, a second threshold K_p is needed to stop the growth. This threshold is not needed in Eq. (12) because local growth stops if nucleation stops.

3.3.3 Quantitative mean-field predictions for p and the Matalon-Packter law

It is possible to calculate the functional dependence of p in the nucleation and growth model described above [32],

$$p = \frac{D_C}{D_f} \left[\frac{c_0}{K_{sp}} - 1 - \frac{D_C}{2D_f} \right]^{-1}. \quad (14)$$

This surprisingly simple analytical solution determines p from the basic parameters D_f and c_0 (from $A + B \rightarrow C$), D_C (for the diffusion of C), and the nucleation threshold K_{sp} . As expected for a mean-field solution, Eq. (14) depends only on dimensionless ratios of the parameters. The first term characterizes the velocity of C versus the velocity of the reaction front, representing a measure of how fast c_0 could be reached. If $D_f \ll D_C$, C will quickly leave the reaction front and diffuse away. In this case it takes longer to reach the desired threshold K_{sp} , and p becomes larger. The second term makes sure that no precipitation occurs if $K_{sp} > c_0$. If K_{sp} is close to c_0 it takes longer to reach K_{sp} and p is also large.

The structure of Eq. (14) will be similar if nucleation and growth is modelled somewhat differently. All mean-field solutions must scale, and patterns emerge only if $K_{sp} \leq c_0$. For this reason Eq. (14) can serve as reference to test further properties of Liesegang pattern formation. One of these properties is the Matalon-Packter law, which is clearly inconsistent with Eq. (14), since it does not scale linearly with $1/a_0$. However, Antal *et al.* [32] could show that the Matalon-Packter law is a special case of Eq. (14), if $b_0 \ll a_0$. Then $D_B \ll D_f$ and the Gaussian error function can be approximated by $\text{erf}(x) \approx 1 - \exp(-x^2) (1 - \frac{1}{2x^2} - \dots) / \sqrt{\pi x}$ [54]. Applying this to Eq. (11) we obtain $c_0 \approx b_0 (1 + \frac{D_B}{D_f}) = b_0 (1 + \frac{D_B}{D_A} \frac{D_A}{D_f})$. In the range $0.05 \leq b_0/a_0 \leq 0.1$ interesting for experiments, Antal *et al.* showed numerically that D_A/D_f is linear in a_0/b_0 . This leads to $D_A/D_f \approx \nu_1 + \nu_2 b_0/a_0$, yielding an approximation for c_0 ,

$$c_0 = b_0 \left(1 + \nu_1 \frac{D_B}{D_A} + \nu_2 \frac{D_B}{D_A} \frac{b_0}{a_0} \right), \quad (15)$$

with $1 + \nu_1 \frac{D_B}{D_A}$ and $\nu_2 \frac{D_B}{D_A}$ numbers of order one. Since $b_0/a_0 \ll 1$ it is possible to neglect the last term in Eq. (15). It is not possible to argue this way already in the linear approximation of D_A/D_f because the ν s do not have the same magnitude. Inserting the approximation back into Eq. (14) we obtain

$$p = \frac{D_C K_{sp} \nu_1}{D_A (\sigma_1 b_0 - K_{sp})} + \frac{D_C K_{sp} \nu_2 b_0}{D_A (\sigma_1 - K_{sp})} \frac{b_0}{a_0} = F(b_0) + G(b_0) \frac{b_0}{a_0}, \quad (16)$$

which is in the form of Eq. (3). The assumptions needed to derive Eq. (16) will be correct for most macroscopic experiments. An important exception might be given by an experiment of nanoscale particles in glasses [1]. In that case a_0 and b_0 have the same magnitude, but D_B seems to be one order of magnitude larger than D_A . This leads to $c_0 \gg b_0$ in contradiction with Eq. (15). However, since only one experiment was carried out yet, we cannot see whether Eq. (14) holds.

3.3.4 The width law

The width law has been neglected in the discussion of Liesegang pattern formation for a long time because of difficulties in defining and measuring the width w_n of the bands consistently. To obtain a finite width in microscopical models one needs to introduce a non-local growth term and a second threshold as $N(c, d)$ from Eq. (13). On the other hand it is also possible to generate a width using Eq. (12) for macroscopic models, e. g. [21].

The first theoretical step in the direction of clarifying the law was done by Droz *et al.* [24] using a model based on Eq. (12). They showed that the total mass m_n of D material in the n th band is proportional to x_n . The concentration profile $d(x, t)$ for $t \gg t_{n+1}$ will be stationary and

has a scaling function of the form, $d_n(x, t) = A_n d[(x - x_n)/w_n]$ for $x_n \leq x \leq x_n + w_n$, where the amplitude A_n could depend on n . It is thus possible to relate m_n with d_n by integration, $m_n = A_n \int_{x_n}^{x_n+w_n} d[(x - x_n)/w_n] dx = \gamma A_n w_n \propto x_n$, where γ is the substituted integral over d_n . Using the first version of Eq. (4), $w_n \sim x_n^\alpha$, this yields $A_n \sim x_n^\beta$ with $\alpha + \beta = 1$ [24]. The authors also discussed experiments, fitting the results with $0.9 < \alpha < 1$.

A more direct treatment was proposed by Racz [23]. Because the $A + B \rightarrow C$ process is independent of the $C \rightarrow D$ process the number of C particles produced in the first process is the same as the number of D particles ending up in the bands. The number of C particles can then be calculated using the assumption that the constant concentration c_0 behind the front is really reached. Later, C precipitates into bands of D with a high concentration d_h while the low concentration c_l of C remains between the bands. The particle conservation law yields $(x_{n+1} - x_n)c_0 = (x_{n+1} - x_n - w_n)c_l + w_n d_h$ leading to the width law in the form

$$w_n = p \frac{c_0 - c_l}{d_h - c_l} x_n \approx p \frac{c_0}{d_h} x_n, \quad (17)$$

since c_l is usually very small. If d_h varies with the band position as $d_h \sim x_n^\beta$ the width law takes again the form $w_n \sim x_n^\alpha$ with $\alpha + \beta = 1$.

3.4 Further reaction-diffusion models and comparison

For charged C particles it is possible to extend the nucleation and growth model such that nucleation only occurs if the concentration of the outer electrolyte A exceeds a third threshold K_a . Such models are known as induced sol coagulation models [11,55,56]. The additional threshold is motivated by the fact that the repulsive electrostatic interaction between the C ions can be screened by A particles. The model yields band formation significantly behind the reaction front as observed in some experiments [12]. The functional form of p deviates from Eq. (14) [32],

$$p = 2 \frac{D_C}{D_f} \left\{ \left[\frac{c_0}{K_{sp}} (1 - K_a/a_0) \right]^2 - \frac{D_C}{D_f} \right\}^{-1}. \quad (18)$$

A fourth category of models is called competitive growth models [16,57,58,59,60,61,62]. In these models, the precipitates D can dissolve with a probability decreasing with increasing size of the precipitates. In special cases it is possible that the bands move [63], dissolve and reprecipitate [15], such that the total number of bands leads to a chaotic time series.

It is possible to compare the F and G functions of the Matalon-Packter law (3) for the supersaturation models with thresholds discussed in Sects. 3.2 to 3.3 and Eq. (18). As already mentioned, the law is valid only for $b_0/a_0 \ll 1$ and $D_B/D_f \leq 1$. The ion product supersaturation model (see Sect. 3.2) predicts $F(b_0) \sim const$ and $G(b_0) \sim K_{sp}/b_0^2$, which is in contradiction to experimental results yielding monotonously decreasing functions of b_0 for F and G [8]. The nucleation and growth model predicts $F(b_0) \sim G(b_0) \sim K_{sp}/(\sigma b_0 - K_{sp}) \approx K_{sp}/b_0$ if $K_{sp} \ll b_0$. The induced sol coagulation model predicts $F(b_0) \sim K_{sp}^2/b_0^2$ and $G(b_0) \sim (\alpha/b_0^3 + \beta/b_0^2)$. In addition, Antal *et al.* [32] remark that a refined version of the sol coagulation model will converge to the nucleation and growth model in the limit $K_a/a_0 \rightarrow 0$. With such a model it should be possible to vary the functional dependence of F such that $F(b_0) \sim b_0^{-\gamma}$ with $1 \leq \gamma \leq 2$, corresponding to $0.2 \leq \gamma \leq 2.7$ observed in experiments, see [32] and references therein. Such refinement is only possible if the C particle are charged. For uncharged C particles the nucleation and growth model still yields the best predictions.

Comparing all four supersaturation models one can conclude that the nucleation and growth model serves best as a reference model. It is the easiest model yielding the Matalon-Packter law. Although it needs an intermediate state C , the model is actually most suitable for analytical and numerical studies. The sol coagulation model and the competitive growth models, on the other hand, can explain details observed in specific experimental setups, but they are not needed to explain the basic universal laws discussed in Sect. 2. The variety of models yielding these

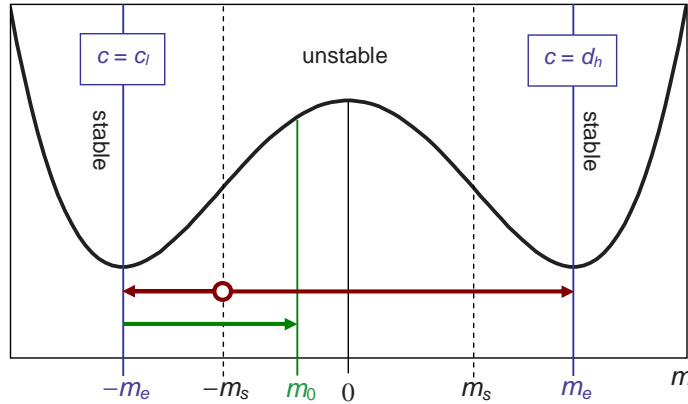


Fig. 4. (colour online) Illustration of the spinodal decomposition model. The homogeneous part of the free energy F is shown as a function of the ‘magnetization’ $m = c - (c_l + d_h)/2$. See text for detailed explanation.

laws is remarkable. The same is true for the variety of physical, chemical and even geological systems showing the phenomenon. This fact suggests that a very general mechanism governs the pattern formation. Such a mechanism will be described in the next section.

3.5 The spinodal decomposition model with Cahn-Hilliard dynamics

Although the supersaturation models described in the previous sections account for most of the Liesegang phenomena, there are drawbacks. Firstly, the threshold parameters controlling the growth of the bands are difficult to grasp theoretically and not easy to control experimentally. Secondly, it is difficult to derive how the band formation could be manipulated in a desired way, since the structure of the models is too complicated. Furthermore, the specific models might seem insufficiently universal. Hence, a new approach free of thresholds and reaction-diffusion equations was recently suggested by Antal *et al.* [27]. They studied only the second process $C \rightarrow D$ of Eq. (5) applying the spinodal decomposition theory for phase separating processes [64,65] to describe the phase separation into bands. We note that the distinction between C and D is actually not necessary here, since the bands correspond to areas with high concentration $c = d_h$, while there is little C between the bands, $c = c_l$ (see also Sect. 3.3.4). Although the model was introduced to describe $C \rightarrow D$ processes it is equally valid for processes where the C particles arrange in bands of high and low concentrations. Then the phase separation is assumed to take place at a very low effective temperature leading to stable bands after long times.

As we have seen in the Sect. 3.3.1 the production of C particles in the $A + B \rightarrow C$ reaction is well understood. The reaction front – an approximately Gaussian shaped region where C is produced at the rate $R(x, t)$ given by Eq. (9) – moves diffusively with its centre at $x_f(t) = \sqrt{2D_f t}$ and its width increasing as $w_f(t) \sim t^{1/6}$. Hence, the spinodal decomposition model can start with the C particles. Their dynamics are described by a simple phase separating equation taking particle conservation into account. The specific dynamics were introduced by Cahn and Hilliard [66,67]. We note that an equivalent approach is the so-called model B in critical dynamics [68].

In the Cahn-Hilliard equation the concentration of C , c , is represented by the so-called ‘magnetization’

$$m = c - (c_l + d_h)/2. \quad (19)$$

Then a Ginzburg-Landau-type free energy is defined in the simplest possible way required for obtaining two minima. This free energy, illustrated in Fig. 4, is finally inserted into the

Cahn-Hilliard equation [23],

$$\partial_t m = -\lambda \partial_x^2 [\epsilon m - \gamma m^3 + \sigma \partial_x^2 m] + R(x, t), \quad (20)$$

Here, $R(x, t)$ is the source term introducing new C particles into the system via the $A + B \rightarrow C$ reaction. The parameters ϵ and γ have to satisfy $\sqrt{\epsilon/\gamma} = (d_h - c_l)/2$, while σ must be positive to eliminate short-wavelength instabilities. λ and σ can be used to set the time-scale and length-scale of the system, which leaves ϵ as the only free parameter. Since ϵ measures the negative deviation of the temperature T from the critical temperature T_c , $\epsilon > 0$ is needed for $T < T_c$. No phase separation occurs for $T > T_c$.

The model can be understood most easily by looking at the free energy sketched in Fig. 4. The source term $R(x, t)$ moves the system from $m = -m_e$ (for $c = c_l \approx 0$) over the spinodal point $-m_s$ to $m = m_0$ which corresponds to $c = c_0$. Choosing m_0 such that it is located in the unstable regime, the system will move to the second stable regime at $m = m_e$ corresponding to the high concentration $c = d_h$, i. e., band formation. The band becomes a sink for C , and its width grows until the front moves away so that m can decay below m_s , and the unstable regime is reached again, moving the system back to $m = -m_e$. Using this model it is possible to produce Liesegang patterns satisfying the spacing law (2) in agreement with the Matalon-Packter law (3) [23,27,69]. Due to the conservation of C particles the arguments regarding the width law presented in Sect. 3.3.4 also apply here. Actually, the derivation of the width law in Eq. (17) was introduced in the context of the spinodal decomposition model.

A special feature not observed in the threshold models is the low density phase with non-zero c , which has been reported in many experiments. The spinodal decomposition model can also be implemented for sophisticated conditions. For example, the effect of an additional electric field was discussed recently this way [42]. However, this can be done similarly using a threshold model [70].

3.6 The kinetic Ising model with Glauber and Kawasaki dynamics

An alternative way to model the phase separating dynamics was recently proposed by Magnin *et al.* [28] along the lines of the kinetic Ising model for ferromagnets. The main advantage is that this model fully describes the fluctuations, going beyond the mean-field approximations. Like in the spinodal decomposition model (see previous section), the concentration of C (and D) particles is represented as a magnetization. The particles are identified as spin-up sites in a cubic lattice, while spin-down sites represent vacancies. Then the formation of precipitates is modelled by a combination of spin-flip and spin-exchange dynamics [71]. The Hamiltonian is the usual nearest neighbour Ising Hamiltonian with ferromagnetic coupling $J > 0$ between the spins $\sigma_{\mathbf{r}}$ at site \mathbf{r} , modelling the attraction of the C particles,

$$H = -J \sum_{\text{neighbours } \mathbf{r}, \mathbf{r}'} \sigma_{\mathbf{r}} \sigma_{\mathbf{r}'}. \quad (21)$$

Specifically, Glauber dynamics [72] are used to add the C particles in an initial state, in which all spins are down. The spin-flip rate $w_{\mathbf{r}}$ at site \mathbf{r} is given by $w_{\mathbf{r}} = R(\mathbf{r}, t)(1 - \sigma_{\mathbf{r}})/2$, with R the source term discussed in Sect. 3.3.1 (see Eq. (9)). Since the width $w_f(t) \sim t^{1/6}$ of the reaction front is not changing much, a constant width leaving behind a constant concentration c_0 of C particles was chosen [28]. The diffusion and interaction of the spin-up sites, i. e., of the particles, is modelled by a spin-exchange process with Kawasaki dynamics [73], $w_{\mathbf{r} \rightarrow \mathbf{r}'} = [1 + \exp(\delta E/(k_B T))]^{-1} / \tau_e$. This exchange rate satisfies a detailed balance at temperature T . The flip frequency τ_e sets the time scale, T is the temperature, k_B the Boltzmann constant, and δE the energy change.

2d and 3d simulations have been reported for this model [28]. In 2d no pattern formation could be found for a wide range of parameters, in contradiction with previous work using lattice-gas simulations [22,25]. In 3d patterns emerge in a restricted parameter range. Due to limited

computational power no quantitative results for Liesegang patterns have been published yet and fluctuations have not been analysed, indicating that the model needs further investigation.

In the next section, we will thoroughly discuss lattice-gas simulations for Liesegang pattern formation, since these studies have already yielded quantitative results and fully include fluctuations.

4 Lattice-gas simulations

In the previous section, we have seen that several mean-field models can reproduce the basic laws of Liesegang pattern formation. However, there are problems not solved by mean-field models.

1. *Is the spacing law valid for all distances or only asymptotically?*
While simple mean-field theories yield $x_n \propto (1+p)^n$ or equivalently $x_{n+1} = (1+p)x_n$, see Sect. 3.2, experimental works usually report an asymptotic behaviour $x_{n+1} \rightarrow (1+p)x_n$ for large n (Eq. (2)).
2. *Which version of the width law is the true one?*
While the mean-field theories generally yield $w_n \propto x_n^\alpha$ (see Eq. (17)), experiments have been fitted successfully by both version of Eq. (4).
3. *Which deviations from the Matalon-Packter law (3) or its more general mean-field form (14) are relevant?*
Although most experimental findings are consistent with the Matalon-Packter law (3), one can expect deviations if D_B is large or if fluctuations become important.
4. *How stable are Liesegang patterns forming under different conditions and in nanoscale systems?*
Simple mean-field models assume the existence of quasi-periodic Liesegang patterns and thus cannot be used to study the stability of the pattern formation process. In general, mean-field quantities like concentrations are not well suited for studying nano-sized systems, since the number of atoms of one agent in a given small volume may fluctuate significantly. These fluctuations can increase or decrease the stability of the Liesegang patterns.
5. *What Liesegang patterns can be expected under special, restricted (e. g., dimensionally reduced), or designed geometries?*
This question is particularly important if self-organization of Liesegang patterns shall be applied to design nanoscale devices. However, mean-field models usually assume a quasi-1d geometry.

In this section we will address problems 1 to 3 by means of lattice-gas simulations. Problems 4 and 5 will be studied in later publications; we just briefly comment on them here.

Problem 4 can be addressed only by models that include the fluctuations of the particle numbers and thus go beyond the mean-field limit. Two major approaches in this direction have been published so far: the kinetic Ising spin simulation reviewed in Sect. 3.6 [28], and lattice-gas simulations on the basis of the nucleation and growth model by Chopard *et al.* [22,25]. Since the Ising model approach is still not so far advanced, we chose the second approach here. An additional advantage is the existence of a corresponding mean-field model (see Sect. 3.3), that the results can be compared with to find out deviations in the universal laws and effects of fluctuations. Equations (14) and (17) represent the mean-field solutions for the spacing law and width law, respectively.

Problem 5 has already been addressed by Liesegang himself since the first experiments were in polar geometry. However, most theoretical work was done in quasi-1d geometry, and nobody investigated how geometry affects the pattern formation and the empirical laws. A first step towards new geometries was done in [2] using mean-field models plus a stochastic term. However, this ansatz seems to be hard to control for some special geometries. Therefore we think that the lattice-gas model can serve as a good candidate to test also new geometries and their influence on the pattern formation.

Lattice-gas simulations can serve as a computational experiment to test how the mean-field solutions can be applied to ‘experimental’ data and furthermore how fluctuations might cause

deviations from these solutions. As suggested by the separation of the two processes in the nucleation and growth model, the lattice-gas simulation consists of two stages. In a first stage the C particles are generated (cf. Sect. 3.3.1). The second stage simulates the precipitation of the C particles by rules comparable with cellular automata (cf. Sect. 3.3.2).

4.1 First process: reaction-diffusion $A + B \rightarrow C$

In the simulation, we consider a simple cubic lattice of size $M \times M \times L$ with $L \gg M$, see Fig. 2(a). Each lattice site represents one cubicle (cell) of the system. Initially, the lattice is homogeneously filled with B particles, i. e., there are on average b_0 independent B particles on each site. The A particles are placed on the left plane of the lattice with a_0 particles on each of the $M \times M$ sites. The parameters a_0 and b_0 can thus be interpreted as concentrations per lattice site. Typically, b_0 is in between 10 and 200, while a_0 is about twice as large. The mean-field limit can be reached if either the considered cells are enlarged or the number of particles per cell is increased. Thus, increasing both a_0 and b_0 but keeping their ratio constant, drives the simulation to the mean-field limit.

The dynamics is modelled as follows. To simulate diffusion, both, A and B particles perform independent random walks on the lattice. The diffusivities D_A and D_B are defined as the probabilities that a motion in either of the six possible directions takes place in a given time step [74,75], i. e., D_A and D_B are proportional to the physical diffusivities. After each time step, the left plane of the lattice is re-filled with A particles with the initial condition. A reaction $A + B \rightarrow C$ takes place with probability κ ($\kappa = 1$ in our simulations), if at least one A and one B particle is found on the same site [51,76]. Afterwards, all C particles also diffuse independently on the lattice with diffusivity D_C . It was previously shown that the mean-field predictions regarding the reaction rate $R(x, t)$ (reviewed in Sect. 3.3.1) are in agreement with the simulations in 3d [51], while logarithmic corrections occur in 2d [76].

Here, we use for the first time 3d lattice-gas simulations for Liesegang patterns in contrast to the 2d setup employed by Chopard *et al.* [22]. For an alternative 3d simulation see Sect. 3.6 [28]. To confirm that the mean-field limit is reached for large concentrations, we ran simulations with different b_0 (keeping a_0/b_0 constant) and found that c_0/b_0 becomes constant in agreement with Eqs. (10) and (11). Figure 5(a) shows the simulated deviations from the mean-field limit, which decay below one percent for $b_0 \gg 2$. We focus on $b_0 > 10$, where the deviations are below 10^{-4} . In a 2d (or 1d) simulation, fluctuations would alter c_0 such that c_0/b_0 does not converge to the mean-field limit even for large b_0 and a_0 [76].

Since the mean-field solutions are valid for a 3d setup, it is possible to insert the C particles directly. This ansatz was first used in a kinetic Ising scenario [28] (see Sect. 3.6). We employ this idea to speed up our numerical calculations, since fully simulating the reaction-diffusion process $A + B \rightarrow C$ reduces the computational speed by at least one order of magnitude. Otherwise we could not work with concentrations $b_0 > 10$ in sensible time. However, this approximation reduces the fluctuations of C particle production, in particular for small concentrations.

The probability to insert C particles into the lattice is given by the reaction rate $R(x, t)$ (see Eq. (9)), with a centre position $x_f(t)$ moving as $x_f(t) = \sqrt{2D_f t}$ to the right. Usually, D_f is calculated via Eq. (10), assuming that the A particles are distributed homogeneously for $x \rightarrow -\infty$, i. e., $a(-\infty, t) = a_{-\infty}$. In this case the A particle concentration outside the quasi-stationary region (see Sect. 3.3.1) can be approximated by $a(x, t) = a_{-\infty} - a_f \left[\operatorname{erf} \left(\frac{x}{2\sqrt{D_A t}} \right) + 1 \right]$ with a constant a_f . However, in our configuration, Eq. (10) needs to be modified, since the concentration of A particles is held constant for all times on the left plane, i. e., for $x = 0$: $a(0, t) = a_{-\infty} - a_f = a_0$. A straightforward derivation similar to the derivation of Eq. (10) in [52] leads to the solution

$$\operatorname{erf} \left(\sqrt{\frac{D_f}{2D_A}} \right) \exp \left(\frac{D_f}{2D_A} \right) = \frac{a_0 \sqrt{D_A}}{b_0 \sqrt{D_B}} H \left[\sqrt{\frac{D_f}{2D_B}} \right]. \quad (22)$$

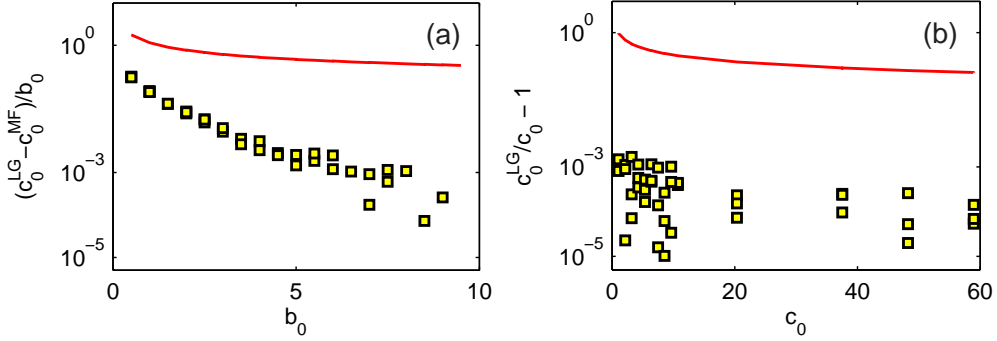


Fig. 5. (colour online) (a) Deviations of the 3d lattice-gas simulations from the mean-field limit. The values of simulated ratios c_0^{LG}/b_0 have been calculated from the plateau of $c(x, t)$ observed behind the diffusion front (see Fig. 3(b)). The corresponding mean-field value c_0^{MF}/b_0 was calculated from Eq. (11). The red curve marks the (scaled) standard deviations of the particle numbers per lattice cell from their means c_0^{LG} indicating the fluctuations in the production of the C particles. The simulation parameters are $a_0/b_0 = 2$, $D_A = 1$, $D_B = 0.1$. (b) Results of our lattice-gas simulations with C particles inserted in an approximated reaction zone according to Eqs. (23) and (24). The values of simulated ratios c_0^{LG}/c_0 have been calculated as in (a). They are in good agreement with the inserted c_0 for all concentrations. Red curve same as for (a). The parameters are $D_f = 1.22$ (calculated from Eq. (22)) and $\Delta = 3$.

Following [28] we approximate the nearly Gaussian-shaped reaction rate term $R(x, t)$ by

$$\tilde{R}(x, t) = \frac{\tilde{A}_f}{\sqrt{t}} \Theta(x - x_f + \Delta) \Theta(x_f + \Delta - x), \quad (23)$$

with constant width 2Δ of the front. These simplifications are justified since the band forming process does not depend on the exact form of the reaction zone [27] and the width of the front increases very slowly in time (as $t^{1/6}$, see Eq. (9)). The most important feature of the reaction front is that it leaves behind a constant concentration c_0 of C particles. Therefore, \tilde{A}_f in Eq. (23) is chosen to be

$$\tilde{A}_f = \frac{\sqrt{2D_f}}{4\Delta} c_0. \quad (24)$$

Figure 5(b) compares the simulated c_0^{LG} with the c_0 value inserted into the simulation via Eq. (24). In contrast to a full simulation of the $A + B \rightarrow C$ reaction (see Fig. 5(a)), c_0^{LG} reaches the mean-field value already for small concentrations since the fluctuations induced by the motion of the A and B particles are eliminated. Only the standard deviation (red curve) of the number of particles per cell is similar as in Fig. 5(a), since the reaction front in (b) is an approximation of the reaction front in (a) and both cause the same fluctuations in C particle production.

4.2 Second process: precipitation $C \rightarrow D$

The second part of our lattice-gas simulation is the precipitation of C particles, generating the immobile precipitate D . The nucleation of D depends only on $c(x, t)$, while the growth of D depends on both, $c(x, t)$ and $d(x, t)$, see also Sect. 3.3.2. In the particle picture of our lattice-gas simulation the density will be the number of particles divided by the considered cell volume. Here, this considered volume around a given lattice cell includes all neighbour cells, i. e., the 27 cells in a cube of $3 \times 3 \times 3$ cells. This definition sets the mean reaction distance.

Two thresholds are introduced. If the mean local concentration of C particles (in the 27 cells) exceeds a threshold K_{sp} , nucleation occurs. C particles in the vicinity of D particles precipitate already if their mean local concentration exceeds a threshold $K_p < K_{sp}$. C particles

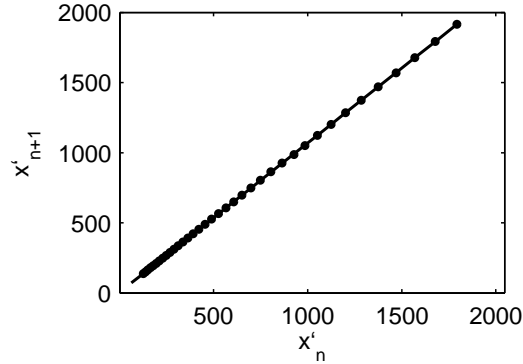


Fig. 6. Spacing law for simulated data depicted in a way different from Fig. 2(b), where x'_{n+1}/x'_n was plotted versus n to observe the asymptotical behaviour (cf. Eq. (26)). Here, x'_{n+1} is plotted versus x'_n to observe the linear behaviour with slope $1 + p$ and offset $p\xi$ (cf. Eq. (27)), yielding $p = 0.066$ and $\xi = 62$. Parameter set for the 3d lattice-gas simulation: $a_0 = 130$, $b_0 = 65$, $D_A = 1$, $D_B = 0.1$ (leading to $D_f = 1.22$ and $c_0/b_0 = 1.072$); $D_C = 0.1$, $K_{sp}/b_0 = 0.93$, and $K_p/b_0 = 0.52$.

on top of D particles always precipitate, which makes the growth process fast enough to deplete a region of C particles. Without this option the growth process would not terminate, and no additional Liesegang bands could be formed. The resulting bands have distinct positions, which we will denote by x'_n in the following; their width is denoted by w_n . We calculated x'_n as the centre of the bands, i. e., the mean of the positions of the first and last D particles within each band. The corresponding widths w_n are defined as the differences between these two positions.

4.3 Reconsideration of the spacing law

Equation (2), i. e., the asymptotical convergence of the ratio of the positions of neighbouring bands $x_{n+1}/x_n \rightarrow 1 + p$ for large n , was estimated from empirical findings; see Sect. 2. On the other hand, theoretical analyses suggest that the ratio x_{n+1}/x_n is identical with $1 + p$ [29,30,31,46], as was discussed in Sects. 3.2 and 3.3. Although these two forms of the spacing law contradict each other, both are still used in parallel without much considerations. We propose a way to reconcile the experimental findings described by the empirical form of the spacing law with the theoretical mean-field prediction.

In experimental and numerical results the position of the first Liesegang band is usually blurred and thus not well defined, contrary to theoretical analyses. Thus, there is an arbitrariness in choosing the position of the first band. Therefore, it is better to use different variables x'_n for the experimentally or numerically measured band positions and x_n for the theoretical positions, since there may be an offset ξ between them,

$$x_n = x'_n + \xi, \quad (25)$$

due to, e. g., the blurred first band. Another possibility is that the mass of D in the first Liesegang band as well as the band's width cannot be close to zero as would be required if the linear increase observed in Fig. 3(c) was beginning at $x' = 0$. We will see later that usually $\xi > 0$, i. e., $x_n > x'_n$, indicating that the ideal laws are based on an 'imaginary' starting point outside the real sample. In literature, however, significant confusion is caused by the fact that both variables, x_n and x'_n , are not distinguished.

Studying measured values x'_n , and assuming both, $x'_n = x_n - \xi$ and the ideal mean-field result, $x_{n+1} = (1 + p)x_n$, one finds the asymptotic (empirical) form of the spacing law,

$$\frac{x'_{n+1}}{x'_n} = \frac{x_{n+1} - \xi}{x_n - \xi} = 1 + p \frac{x_n}{x_n - \xi} = 1 + p \frac{x'_n + \xi}{x'_n} = 1 + p + \frac{p\xi}{x'_n} \rightarrow (1 + p) \quad (26)$$

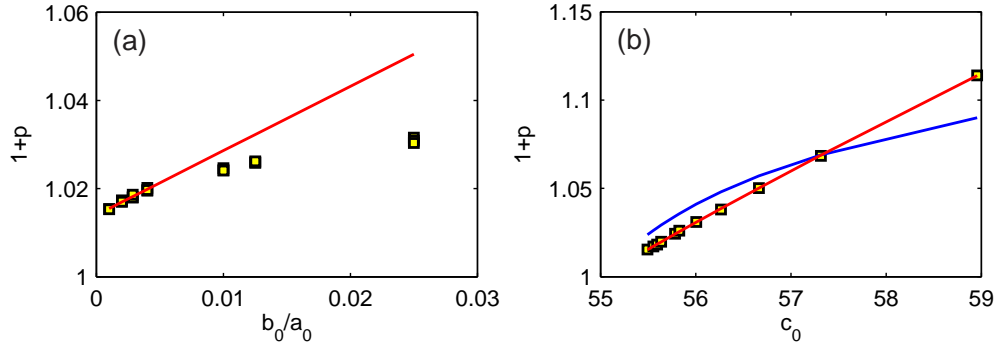


Fig. 7. (colour online) Reconsideration of the Matalon-Packter law based on 3d lattice-gas simulations. (a) The yellow squares indicate simulation results for the spacing law coefficient p obtained keeping b_0 constant and varying a_0 . The straight line is a linear fit to the first four data points using Eq. (3). (b) Simulation results similar to those shown in (a). D_f and c_0 are calculated using Eqs. (22) and (11), respectively. The blue curve is a fit of Eq. (14), while the red curve takes fluctuations into account. Parameters: $b_0 = 55$, $D_A = 1$, $D_B = 0.1$, $D_C = 0.15$, $K_{sp}/b_0 = 0.96$, and $K_p/b_0 = 0.52$.

for large n as in Eq. (2). Figure 2(b) shows this asymptotic behaviour as observed in simulated data; note that actually the values of x'_n rather than x_n are plotted. The coefficient p is hard to determine in such plots, especially if only few bands are present. A more convenient way to extract p from measured data is to fit the equation

$$x'_{n+1} = (1+p)x'_n + p\xi, \quad (27)$$

where $p\xi$ is the intersection with the ordinate, as shown in Fig. 6 for the same data. Even for a small number of bands, p and ξ can be extracted conveniently. In addition, we believe that the offset ξ is an important ingredient that should not be neglected in interpreting any experimental or simulated data. However, it remains unclear if or how the value of ξ could be predicted.

4.4 Reconsideration of the Matalon-Packter law

The original Matalon-Packter law (3) predicts a linear dependence between b_0/a_0 and p . It was shown in Sect. 3.3.3 that this empirical law holds for $b_0 \ll a_0$ only. In addition, a more general law was presented in Eq. (14) [32]. The deviations from Eq. (3) are even stronger in the results of lattice-gas simulations. An example is depicted in Fig. 7(a). A linear dependence is observed only for $a_0/b_0 > 250$, a criterion shown to be equivalent to $D_B/D_f \approx 1$ [32]. If a_0 is reduced for constant b_0 , D_f increases, driving the system out of the regime in which Eq. (3) is valid [32]. Our lattice-gas simulations confirm these results, see Fig. 7(a).

Figure 7(b) compares a fit of the generalized Matalon-Packter law Eq. (14) (blue curve) with the results of our lattice-gas simulations. The deviations are still quite large. Only if fluctuations are taken into account by further modifying the generalized Matalon-Packter law, a nice agreement can be reached. The formula used for the red fit in Fig. 7(b) will be discussed and motivated in detail in a later publication.

4.5 Reconsideration of the width law

As discussed in Sect. 2 two competing empirical forms of the width law are used for fitting experimental data,

$$w_n = \mu_1 x_n + \mu_2 \quad \text{and} \quad w_n \propto x_n^\alpha. \quad (4)$$

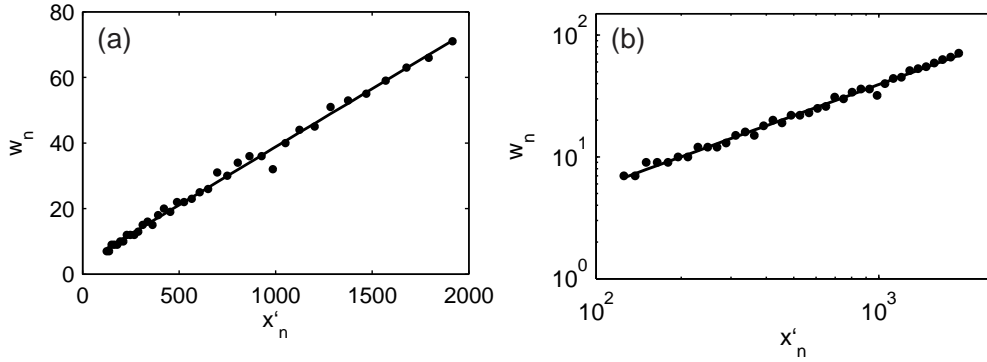


Fig. 8. Reconsideration of the width law based on 3d lattice-gas simulations. (a) Linear presentation of w_n versus x'_n (points) together with a fit of the first version of Eq. (4) with $\mu_1 = 0.035$ and $\mu_2 = 3.4$. (b) Double logarithmic presentation of the same data together with a fit of the second version of Eq. (4) with slope $\alpha = 0.82$. The same simulation as for Figs. 2 and 6 was used.

Figure 8 shows the results of our lattice-gas simulations in both representations, because w_n is plotted versus x'_n both linearly and double logarithmically. Clearly, it is not possible to favour either of the two forms of the width law, since all widths are small compared with the size of the sample and both fits have an equivalent quality.

On the other hand, in Sect. 3.3.4 a simple and general width law was deduced theoretically (see Eq. (17)) using particle conservation. Assuming scaling behaviour of the band densities d_n , $d_n \propto x_n^\beta$, and setting $c_l = 0$ (since no precipitate occurs between the bands in our simulation), one obtains

$$w_n = p \frac{c_0}{d_n} x_n \propto x_n^\alpha \quad (28)$$

with $\alpha = 1 - \beta$. This law was derived using the theoretical x_n where the ratio for two consecutive bands is constant, i. e., the exact form of the spacing law. A width law valid for experimental or numerical data of the positions x'_n of the bands can be derived introducing the offset ξ , see Eq. (25). The analytical form of the width law thus becomes

$$w_n = p \frac{c_0}{d_n} (x'_n + \xi) = p \frac{c_0}{d_n} x'_n + \frac{c_0}{d_n} p \xi, \quad (29)$$

which is in between the two competing empirical forms (4), since $d_n \propto (x'_n + \xi)^\beta$. Note that $p\xi$ is identical with the offset of the fit for the spacing law (27). Hence, the parameter ξ is also important for understanding the width law.

To test these predictions we have run simulations and fitted Eq. (28) to extract α from the data disregarding ξ , i. e., inserting x'_n directly for x_n . The results are shown in Fig. 9(a), yellow points. In a second approach we used the same data and inserted $x_n = x'_n + \xi$ into Eq. (28), also obtaining α as a fit parameter. The results are shown in Fig. 9(a), red points. Both approaches lead to different values of α indicating that the offset ξ plays a significant role.

Since the width law depends on the density of the bands d_n , it is not possible to distinguish the correct form by just looking at the width exponent α . Therefore, we have also calculated the densities d_n in the numerical simulations. Figure 9(b) shows the exponent β obtained by fitting $d_n \propto x_n'^\beta$ (yellow points) and $d_n \propto (x'_n + \xi)^\beta$ (red points). In addition, Fig. 9(c) depicts the sum of both exponents from parts (a) and (b), $\alpha + \beta$. The product $w_n d_n$ can be interpreted as the mass m_n of band n ; it scales as $m_n = p c_0 x_n = p c_0 x'_n + p c_0 \xi$ according to Eq. (29). Thus, according to theory, the mass exponent $\alpha + \beta$ must be one. The results shown in Fig. 9(c) indicate that this holds only in the case where the offset ξ is taken into account correctly (red points), confirming that ξ must not be disregarded.

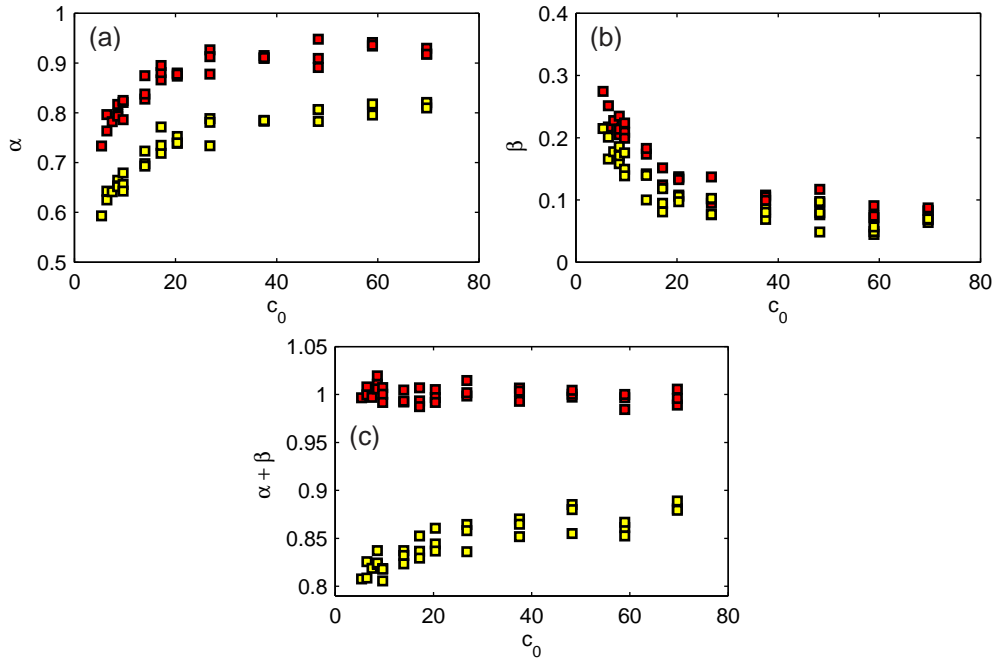


Fig. 9. (colour online) Fits of (a) width, (b) density, and (c) mass scaling behaviour based on our 3d lattice-gas simulations for different values of c_0 . The exponents have been obtained by fitting a power-law to plots of (a) w_n , (b) d_n , and (c) $m_n = d_n w_n$ versus x'_n (yellow dots) and versus $x'_n + \xi$ (red dots). The parameters of the simulations are identical with those used for Figs. 2 and 6, except for varied c_0 .

4.6 Application to previous experimental data

We believe that much confusion in literature could be avoided if the difference between x_n and x'_n was taken into account. In particular, the long-standing discussion about the width law could probably be solved if the analysis of experimental data included plots versus $x_n = x'_n + \xi$. We suggest that former experiments should be re-analysed using ξ and x'_n to confirm our conclusions.

An experiment which confirms the result of Eq. (29) was published recently [19]. The authors investigated pattern formation in a κ -Carrageenan gel. They measured x'_n and w_n for different concentration of the outer solution. First they plotted x'_{n+1} versus x'_n in a fashion similar to Fig. 6 and extracted p . Looking at the plot, we can clearly see offsets corresponding to $p\xi$. Secondly they plotted w_n versus x'_n in a linear fashion similar to Fig. 8(a), extracting the parameter $\mu_1 = pc_0/d_n$ in Eq. (29), assuming constant densities d_n . Looking at the plot, we also clearly see offsets corresponding to $\mu_2 = p\xi c_0/d_n$ (according to Eq. (29)). In addition they determined $c_0/d_n = 0.53$. This means that the offsets of the width law must be approximately half of the offsets of the spacing law. This conclusion is in quantitative agreement with the offsets we read from the plots in [19]. The experimental data thus confirm our conclusion that the offset ξ should be taken into account.

The differences of Eqs. (17) and (29) explain the different approaches used in experiment and theory. In summary, we have solved problems 1 and 2 raised in the beginning of Sect. 4; problem 3 was discussed in Sect. 4.4.

5 Summary and outlook

In this paper we reviewed the four empirical laws believed to govern Liesegang pattern formation and several important mean-field models reproducing these laws as well as a few Monte-Carlo-

type simulations. Based on our detailed 3d lattice-gas simulations of the nucleation and growth model, we detected three major problems in reconciling the experimental reports with mean-field results. However, our simulations also helped us to find a straightforward solution.

We have shown that all basic empirical laws describing Liesegang pattern formation, i. e., the time law, the spacing law, the Matalon-Packter law, and the width law can be understood on the basis of the nucleation and growth model. A full agreement between experimental observations, simulation results, and mean-field models can be obtained only if a constant offset ξ between measured and theoretically assumed band positions is taken into account, as suggested in this work. A re-analysis of a previous experiment concerning the spacing law and the width law confirmed our suggestion. We propose that further experiments should be re-analysed to test the refined predictions.

In addition, we suggest further experiments with systematically varied concentrations of both, inner and outer electrolyte to confirm or extend the generalized Matalon-Packter law (14). Our current work in progress regarding the effects of fluctuations on Liesegang pattern formation indicates that additional modifications of the Matalon-Packter law are necessary in small-scale systems. Reliable experimental results for the nanoscale regime, where fluctuations are definitely important, are expected to become available soon, since experiments with nanoscale particles get feasible. A big open question will be how to manipulate the pattern formation such that interesting nanoscale devices could be designed. A deeper understanding of the dynamics is important for reaching this goal. For a first promising work in this direction, see [43].

We thank I. Bena, M. Droz, M. Dubiel, I. L'Heureux, Y. Kaganovskii, I. Lagzi, K. Martens, and M. Rosenbluh for discussions. We would like to acknowledge support of this work from the Deutsche Forschungsgemeinschaft (DFG, project B16 in SFB 418).

References

1. C. Mohr, M. Dubiel, and H. Hofmeister, *J. Phys.: Condens. Matter* **13**, 525 (2001).
2. I. T. Bensemann, M. Fialkowski, and B. A. Grzybowski, *J. Phys. Chem. B* **109**, 2774 (2005).
3. B. A. Grzybowski, K. J. M. Bishop, C. J. Campbell, M. Fialkowski, and S. K. Smoukov, *Soft Matter* **1**, 114 (2005).
4. R. E. Liesegang, *Naturw. Wochschr.* **11**, 353 (1896).
5. W. Ostwald, *Lehrbuch der Allgemeinen Chemie* (Engelmann, Leipzig, 1897).
6. H. W. Morse and G. W. Pierce, *Phys. Rev.* **17**, 129 (1903).
7. K. Jablczynski, *Bull. Soc. Chim. France* **33**, 1592 (1923).
8. R. Matalon and A. Packter, *J. Colloid Sci.* **10**, 46 (1955).
9. A. Packter, *Kolloid-Z.* **142**, 109 (1955).
10. H. Hensch, *Crystals in Gels and Liesegang Rings* (Cambridge University Press, 1988).
11. S. Shinohar, *J. Phys. Soc. Jpn.* **29**, 1073 (1970).
12. S. Kai, S. C. Müller, and J. Ross, *J. Chem. Phys.* **76**, 1392 (1982).
13. S. C. Müller, S. Kai, and J. Ross, *J. Phys. Chem.* **86**, 4078 (1982).
14. M. E. Levan and J. Ross, *J. Phys. Chem.* **91**, 6300 (1987).
15. R. F. Sultan, *Phys. Chem. Chem. Phys.* **4**, 1253 (2002).
16. J. George and G. Varghese, *Chem. Phys. Lett.* **362**, 8 (2002).
17. S. C. Müller and J. Ross, *J. Phys. Chem. A* **107**, 7997 (2003).
18. J. George and G. Varghese, *J. Colloid Interface Sci.* **282**, 397 (2005).
19. T. Narita and M. Tokita, *Langmuir* **22**, 349 (2006).
20. In the original work, the Matalon-Packter law was introduced as $p = F(b_0) + G(b_0)/a_0$. The disadvantage of this equivalent definition is that $G(b_0)$ gets the dimension of b_0 .
21. G. T. Dee, *Physica D* **23**, 340 (1986).
22. B. Chopard, P. Luthi, and M. Droz, *J. Stat. Phys.* **76**, 661 (1994).
23. Z. Racz, *Physica A* **274**, 50 (1999).
24. M. Droz, J. Magnin, and M. Zrinyi, *J. Chem. Phys.* **110**, 9618 (1999).
25. B. Chopard, P. Luthi, and M. Droz, *Phys. Rev. Lett.* **72**, 1384 (1994).
26. J. Crank, *The Mathematics of Diffusion* (Oxford Science Publications, Oxford, 1996).
27. T. Antal, M. Droz, J. Magnin, and Z. Racz, *Phys. Rev. Lett.* **83**, 2880 (1999).

28. T. Antal, M. Droz, J. Magnin, A. Pekalski, and Z. Racz, *J. Chem. Phys.* **114**, 3770 (2001).
29. C. Wagner, *J. Coll. Sci.* **5**, 85 (1950).
30. S. Prager, *J. Chem. Phys.* **25**, 279 (1956).
31. Y. Zeldovich, R. L. Salganik, and G. I. Barenblatt, *Dokl. Akad. Nauk* **140**, 1281 (1961).
32. T. Antal, M. Droz, J. Magnin, Z. Racz, and M. Zrinyi, *J. Chem. Phys.* **109**, 9479 (1998).
33. M. I. Lebedeva, D. G. Vlachos, and M. Tsapatsis, *Phys. Rev. Lett.* **92**, 088301 (2004).
34. F. Izsak and I. Lagzi, *J. Chem. Phys.* **122**, 184707 (2005).
35. F. Izsak and I. Lagzi, *J. Chem. Phys.* **120**, 1837 (2004).
36. S. K. Smoukov, A. Bitner, C. J. Campbell, K. Kandere-Grzybowska, and B. A. Grzybowski, *JACS* **127**, 17803 (2005).
37. B. Chopard, M. Droz, J. Magnin, Z. Racz, and M. Zrinyi, *J. Phys. Chem. A* **103**, 1432 (1999).
38. M. Msharrafieh and R. Sultan, *Chem. Phys. Lett.* **421**, 221 (2006).
39. I. Lagzi and F. Izsak, *Phys. Chem. Chem. Phys.* **7**, 3845 (2005).
40. I. Lagzi and F. Izsak, *Phys. Chem. Chem. Phys.* **5**, 4144 (2003).
41. Z. Shreif, L. Mandalian, A. Abi-Haydar, and R. Sultan, *Phys. Chem. Chem. Phys.* **6**, 3461 (2004).
42. I. Bena, M. Droz, and Z. Racz, *J. Chem. Phys.* **122** (2005).
43. T. Antal, I. Bena, M. Droz, K. Martens, and Z. Racz, *Phys. Rev. E* **76** (2007).
44. A. Buki, E. Karpatismidroczi, and M. Zrinyi, *J. Chem. Phys.* **103**, 10387 (1995).
45. In the original paper the second term was not introduced as a formula but described in the text.
46. J. B. Keller and S. I. Rubinow, *J. Chem. Phys.* **74**, 5000 (1981).
47. Y. Kaganovskii, A. Lipovskii, M. Rosenbluh, and V. Zhurikhina, *J. Non-Cryst. Solids* **353**, 2263 (2007).
48. For our problem we will need the additional boundary condition $a(0, t) = a_0$. The changes needed to achieve this will be introduced in Sect. 4.1.
49. L. Galfi and Z. Racz, *Phys. Rev. A* **38**, 3151 (1988).
50. H. Larralde, M. Araujo, S. Havlin, and H. E. Stanley, *Phys. Rev. A* **46**, R6121 (1992).
51. S. Cornell, M. Droz, and B. Chopard, *Phys. Rev. A* **44**, 4826 (1991).
52. Z. Koza, *J. Stat. Phys.* **85**, 179 (1996).
53. M. Fialkowski, A. Bitner, and B. A. Grzybowski, *Phys. Rev. Lett.* **94** (2005).
54. *Handbook of Mathematical Functions with Formulas, Graphs, and Mathematical Tables*, edited by M. Abramowitz and I. A. Stegun (Dover Publications, 1972).
55. N. Chatterji and N. Dhar, *Kolloid-Z.* **31** (1922).
56. N. Dahr and A. Chatterji, *J. Phys. Chem.* **28**, 41 (1924).
57. M. Flicker and J. Ross, *J. Chem. Phys.* **60**, 3458 (1974).
58. R. Feeney, S. L. Schmidt, P. Strickholm, J. Chadam, and P. Ortoleva, *J. Chem. Phys.* **78**, 1293 (1983).
59. G. Venzl, *J. Chem. Phys.* **85**, 1996 (1986).
60. D. S. Chernavskii, A. A. Polezhaev, and S. C. Müller, *Physica D* **54**, 160 (1991).
61. M. Chacron and I. L'Heureux, *Phys. Lett. A* **263**, 70 (1999).
62. H. J. Krug and H. Brandtstadter, *J. Phys. Chem. A* **103**, 7811 (1999).
63. M. Zrinyi, L. Galfi, E. Smidroczi, Z. Racz, and F. Horkay, *J. Phys. Chem.* **95**, 1618 (1991).
64. J. D. Gunton and M. Droz, *Introduction to the Theory of Metastable and Unstable States* (Springer, 1983).
65. *Phase Transition and Critical Phenomena*, edited by C. Domb and J. L. Lebowitz (Academic Press, 1982).
66. J. W. Cahn and J. E. Hilliard, *J. Chem. Phys.* **28**, 258 (1958).
67. J. W. Cahn, *Acta Metall.* **9**, 795 (1961).
68. P. C. Hohenberg and B. I. Halperin, *Rev. Mod. Phys.* **49**, 435 (1977).
69. M. Droz, *J. Stat. Phys.* **101**, 509 (2000).
70. I. Bena, F. Coppex, M. Droz, and Z. Racz, *J. Chem. Phys.* **122** (2005).
71. M. Droz, Z. Racz, and J. Schmidt, *Phys. Rev. A* **39**, 2141 (1989).
72. R. J. Glauber, *J. Math. Phys.* **4**, 294 (1963).
73. K. Kawasaki, *Phys. Rev.* **145**, 224 (1966).
74. B. Chopard and M. Droz, *J. Stat. Phys.* **64**, 859 (1991).
75. T. Kkarapiperis and B. Blankleider, *Physica D* **78**, 30 (1994).
76. B. Chopard and M. Droz, *Europhys. Lett.* **15**, 459 (1991).